Chemical Science

ROYAL SOCIETY OF CHEMISTRY

EDGE ARTICLE

View Article Online
View Journal | View Issue

Cite this: *Chem. Sci.*, 2024, **15**, 13788

All publication charges for this article have been paid for by the Royal Society of Chemistry

The molecular basis for the increased stability of the FUS-LC fibril at the anionic membrane- and air–water interfaces†

Sanjoy Paul,[a] Sayantan Mondal,[a] Irina Shenogina[b] and Qiang Cui *[ac]

Self-organization of biomolecules can lead to the formation of liquid droplets, hydrogels, and irreversible aggregates that bear immense significance in biology and diseases. Despite the considerable number of studies conducted on biomolecular condensation in bulk solution, there is still a lack of understanding of how different surfaces regulate the condensation process. In this context, recent studies showed that, in contrast to zwitterionic lipid membranes, anionic membranes promoted the production of liquid droplets of FUsed in Sarcoma Low Complexity domain (FUS-LC) despite exhibiting no specific protein-lipid interactions. Moreover, the air–water interface led to a solid fibril-like aggregate of FUS-LC. The molecular mechanism of condensation/aggregation of proteins in response to surfaces of various charged states or levels of hydrophobicity remains to be better elucidated. Here, we provide initial insights into this question by investigating the stability of a small β fibril state of FUS-LC in bulk solution *vs.* membrane- and air–water interfaces. We perform multiple independent molecular dynamics simulations with distinct starting conformations for each system to demonstrate the statistical significance of our findings. Our study demonstrates the stability of the FUS-LC fibril in the presence of anionic membranes on the μs timescale while the fibril falls apart in bulk solution. We observe that a zwitterionic membrane does not enhance the stability of the fibril and 1,2-dioleoyl-*sn*-glycero-3-phospho-L-serine (DOPS) has a higher propensity to stabilize the fibril than dioleoylphosphatidylglycerol (DOPG), in qualitative agreement with experiments. We further show that the fibril becomes more stable at the air–water interface. We pinpoint interfacial solvation at the membrane- and air–water interfaces as a key factor that contributes to the stabilization of the peptide assembly.

Received 5th April 2024
Accepted 22nd July 2024

DOI: 10.1039/d4sc02295e

rsc.li/chemical-science

1 Introduction

Liquid liquid phase separation (LLPS) of intrinsically disordered peptides (IDPs) and nucleic acids has emerged as a vital and ubiquitous phenomenon that regulates various cellular processes such as transcription, genome organization, immune response and many more.[1–3] LLPS derived biomolecular condensates (BCs) may transform into stable aggregated states that are linked to various neuro-degenerative diseases.[4,5] Although LLPS induces cellular compartmentalization in a membraneless manner, cells contain various membrane enclosed organelles, and how membranes of these organelles regulate the localization and properties of the condensates remains an active topic of research.[6–8] Membranes have been shown to promote cluster/aggregate formation of disordered proteins through both specific[9–12] and non-specific protein-lipid interactions.[13–20] For example, anionic membrane mediated secondary nucleation is identified as a key step for the membrane induced aggregation of IAPP.[21] Further, helix dipole of IAPP is considered to play an important role in the membrane mediated self assembly pathway.[22] Apart from membranes, hydrophobic surfaces are also known to be the driver of biomolecular aggregation.[23] A unifying molecular mechanism that explains biomolecular condensation in the presence of surfaces of different levels of hydrophobicity and charge patterning is yet to be established.

FUsed in Sarcoma (FUS) is a RNA binding protein implicated in neurological disorder.[24,25] Its N-terminal Low Complexity (FUS-LC) domain, which is rich in QSYG repeat, is known to undergo LLPS when the concentration reaches a threshold value.[26,27] In the canonical liquid droplet, FUS-LC maintains a dynamic, disordered structure that involves multivalent interactions among various residue types.[26] FUS-LC also forms amyloid like fibril with an S bent topology by its N-terminal residues 39–95 (ref. 28) and a U shaped fibril with residues 112–150.[29,30] Recent experiments revealed that anionic lipid membranes induce the liquid droplet formation at

[a]*Department of Chemistry, Boston University, 590 Commonwealth Avenue, Massachusetts-02215, USA*

[b]*Department of Physics, University of Illinois Urbana-Champaign, USA*

[c]*Departments of Physics, and Biomedical Engineering, Boston University, Massachusetts-02215, USA. E-mail: qiangcui@bu.edu*

† Electronic supplementary information (ESI) available. See DOI: https://doi.org/10.1039/d4sc02295e

a concentration that is ~30 fold lower than that required for bulk phase condensate formation (FUS-LC residues 1–163).[20] In that study, a zwitterionic lipid membrane (DOPC) did not lead to any droplet formation whereas a DOPS (anionic) membrane specifically gave rise to β-sheet like ordering of FUS-LC. At the air–water interface, the same FUS-LC region forms solid fibril like aggregates at an even lower concentration.[23] Interestingly, aging of the liquid droplet state can lead to a multiphase architecture[31] where surface of the droplet plays a crucial role.[32–34] It remains unclear in molecular level details how different interfaces influence the condensation of FUS-LC.

One common feature for the anionic membrane surface and the air/water interface is that water molecules therein have strongly preferred orientations[35,36] These aligned water molecules together with nearby charged groups (*e.g.*, phosphate groups in the lipids) can lead to significant local electric fields. For example, organic surfactant molecules were shown to induce local alignment of water molecules where an effective electric field of ~1 V nm^{-1} emerges from both surfactant and water molecules.[37] The unique solvent distributions at these interfaces also perturb intermolecular interactions between solutes. For instance, it was demonstrated that oppositely charged ion-pairs become more attractive and like-charged ion-pairs less repulsive at the air–water interface compared to the bulk.[38] Therefore, it is important to analyze the potential contributions of interfacial solvent and electric field distributions to the assembly of IDPs such as FUS-LC.

Motivated by such considerations, we perform multiple replica atomistic molecular dynamics (MD) simulations of FUS-LC in the presence of membrane-water and air–water interfaces to understand how these surfaces modulate the stability of the fibrillar assembly of the peptides. We extract a β fibrillar assembly of FUS-LC comprising residues 112–130 from the U-shaped hairpin structure, which dissociates into a collapsed state in a computationally tractable time-window. In the presence of membrane composed of anionic lipids, FUS-LC maintains its hydrogen bonded assembly whereas a membrane composed of zwitterionic lipids is unable to maintain the structural integrity of the β strands. The air–water interface also leads to enhanced stability of FUS-LC compared to the bulk solution. To better understand the effect of interface, we apply an external static electric field in bulk solution to mimic the interface-like water alignment and compare the stability of the peptide assembly in the absence and presence of the electric field. Additionally, we calculate the potentials of mean force (PMFs) for the association of simple molecular/ionic systems near different surfaces to illustrate the effect of an interface on the free-energy profile. Overall, our simulations provide evidence for the strengthening of hydrogen bonded networks in peptide assembly due to the distinct interfacial solvent distributions at the membrane/air–water interfaces.

2 Methods

2.1 Atomistic molecular dynamics simulations in bulk solution and in the presence of membrane

We start with the cryo-EM structure of the U-shaped β hairpin aggregate of FUS-LC (PDB code: 6XFM)[29] formed by residues 112–150 and consider four of its fragment copies (Fig. 1A) for simulation. To prepare a planar β fibril aggregate (as shown in Fig. 1C–E) with a shorter segment of the peptide, we consider only the first 19 residues in each of the peptides and replicate the coordinates to establish an eight-fragment assembly. We perform all-atom MD simulations using GROMACS version 2020.6 (ref. 39 and 40) and the CHARMM36m force field[41] with the TIP3P explicit solvent model. The systems are prepared using CHARMM-GUI.[42–44] The β hairpin aggregate is placed at the center of a ~10 × 10 × 10 nm^3 box. For the periodic arrangement of β fibril (as shown in Fig. 1C), we maintain the box size as ~6 × 3 × 16 nm^3; the *Y* dimension is shrank to the dimension of the fibril so that the peptides at the edge form hydrogen bonds with their periodic images. We employ semi-isotropic pressure coupling here. In another simulation setup, the periodic continuity of the fibril is disrupted by considering a cubic box of size ~8.7 × 8.7 × 8.7 nm^3 as shown in Fig. 1E and isotropic pressure coupling is applied.

We neutralize the systems and maintain the physiological (0.15 M) salt concentration by adding Na^+ and Cl^- ions. The Particle Mesh Ewald[45] (PME) method is used to compute the electrostatic interactions and a switching function is used to reduce the van der Waals force smoothly to zero between 1.0 and 1.2 nm. The solvated system is first energy-minimized using the conjugate gradient approach. Afterwards, a brief *NVT* equilibration is conducted in which the protein atoms are first subjected to a harmonic restraint and then progressively relaxed. This *NVT*-equilibrated system is then subjected to *NPT* production run for 1 μs at the atmospheric pressure and 303 K temperature, during which no atoms are restrained. The temperature of the system during equilibration is controlled by the Nosé–Hoover thermostat[46,47] with a time constant of 1 ps. The Parrinello–Rahman barostat[48] with a time constant of 5 ps is employed during the production run to maintain the pressure of the system to 1 bar. The LINCS algorithm[49] is used to constrain covalent bonds involving hydrogen atoms to enable an integration time step of 2 fs.

To assess the impact of lipid membrane on the structure and dynamics of the FUS-LC fibril, three types of lipid membranes are explored, which are composed of 1,2-dioleoyl-*sn*-glycero-3-phosphocholine (DOPC), 1,2-dioleoyl-*sn*-glycero-3-phospho-L-serine (DOPS) or dioleoylphosphatidylglycerol (DOPG). Each simulation system has an area of ~10 × 10 nm^2 and contains ~280 lipids. We explore five starting orientations of the fibril (Fig. S1†) with respect to the membrane surface and the *Z* dimension of the simulation box varies accordingly between 10–14 nm. In each case, we run 1 μs *NPT* production run after a short *NVT* equilibration as described in the previous case.

2.2 Atomistic molecular dynamics simulations in the presence of the air–water interface

To prepare a system containing the air–water interface, we start with a previously equilibrated bulk solvent box of size ~8.7 × 8.7 × 8.7 nm^3 and increase the size of the *Z* dimension to 18 nm. Under PBC condition this set up creates a vacuum layer of ~10 nm along the *Z* axis (Fig. 3A). We place the peptides at

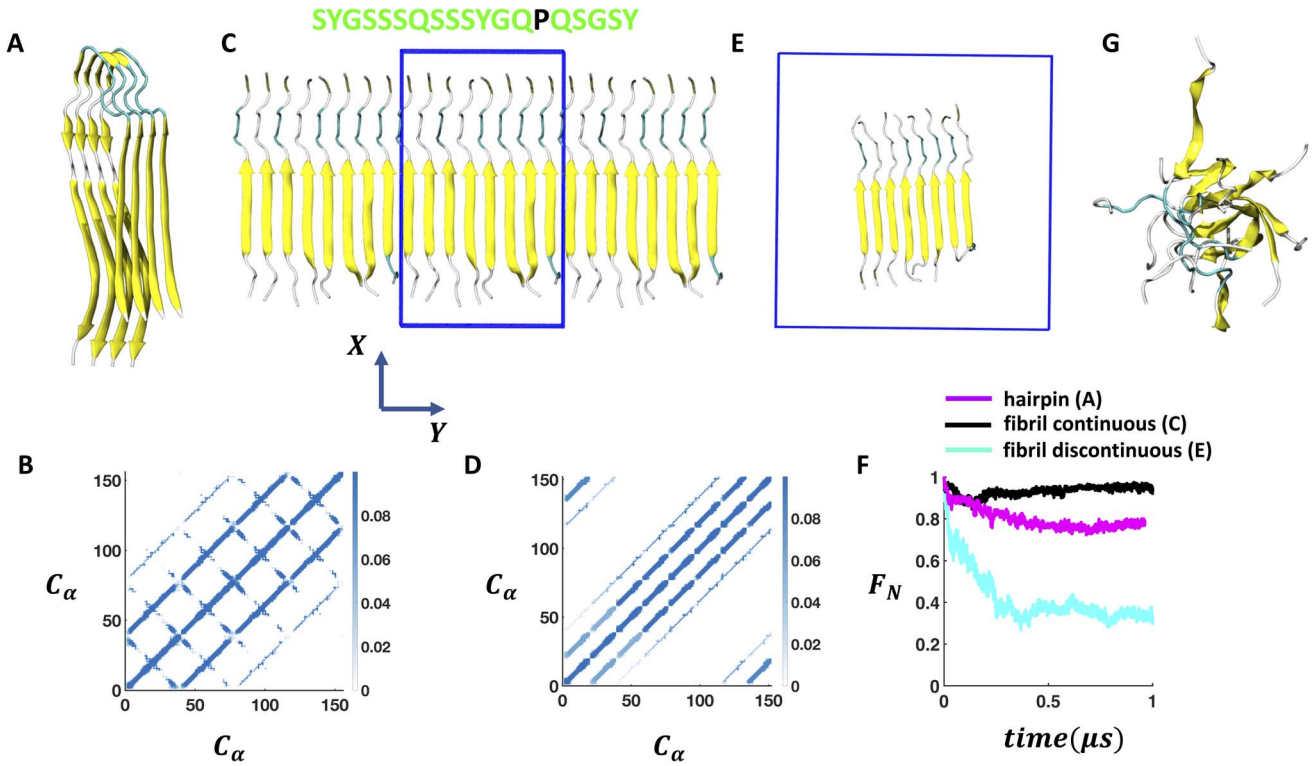

Fig. 1 Stability of the self-assembled FUS-LC aggregate in bulk solution. (A) Experimentally (PDB code: 6XFM) derived U bend topology of FUS-LC exhibited by residues 112–150. The four fragment copies of β hairpin structures remain stable on the μs timescale during MD simulations. (B) Trajectory averaged contact map (10 Å cutoff) of the structure shown in A considering only Cα atoms. (C) The β hairpin aggregate is converted into a planar 8 fragment β fibril structure (residue 112–130) where size of the solvent box (blue box) is adjusted to maintain the continuity of the fibril with its periodic images along the *Y* direction. Periodic images of the fibril along +*Y* and −*Y* directions are also shown. Amino acid sequence of the each peptide is shown at the top where hydrophilic residues are coloured in green and hydrophobic residues are coloured in black. (D) Contact map of the structure shown in B considering only Cα atoms. (E) Extra solvent padding is added to make the 8-fragment fibril periodically discontinuous. (F) Time evolution of the fraction of native contacts of the structure shown in A, C, and E indicates a significant loss of stability in the case of E compared to A and C. (G) Structure of the discontinuous fibril after 1 μs of MD simulation.

the air–water interface and perform 1 μs NVT production runs with different conditions. First, no positional restraint is applied to the peptide or water molecules (bulk-2 in Fig. 3). Next, we apply a flat bottom positional restraint on the backbone atoms of the peptides (bulk-3 in Fig S5–S7†) such that movement of the peptide atoms are restricted within a layer of 3 nm thickness along the *Z* dimension with a force constant of 3000 kJ mol^{-1} nm^{-2}. Without any restraints on the water molecules, they readily wrap around the peptides, creating a bulk-like environment. To maintain a solvation environment of the peptide characteristic of the air–water interface, we apply restraints on the water molecules (Fig. 3) to prevent them from fully solvating the peptides. The restraints are flat bottom in nature with the following functional form:

$$V_{\mathrm{fb}} = \frac{1}{2} \times k_{\mathrm{fb}} \times \left(|z_i - z_{\mathrm{center}}| - \frac{1}{2} \times z_{\mathrm{length}} \right)^2 \times H\left(|z_i - z_{\mathrm{center}}| - \frac{1}{2} \times z_{\mathrm{length}} \right) \quad (1)$$

where k_{fb} is taken to be 3000 kJ mol^{-1} nm^{-2}, z_i is the *Z* coordinate of the *i*th water oxygen, z_{center} is the *Z* coordinate of the center of the solvent slab, z_{length} is the thickness of the solvent slab and *H* is the Heaviside step function. Water molecule inside the solvent slab $\left(|z_i - z_{\mathrm{center}}| < \frac{1}{2} \times z_{\mathrm{length}} \right)$ are free from any restraining potential and can readily form hydrogen bonds with other water molecules and available peptide residues. Considering the large value of z_{length} (7.6 nm), the impact of the restraining potential on water molecules near the peptide is expected to be minimal. Additional simulations (interface 1–3) with different water restraints are also explored and included in the ESI as additional controls (Fig. S8–S10).†

2.3 Bulk simulation in the presence of an external electric field

To assess the impact of aligned water molecules and enhanced local electric field on the stability of the fibril, we perform MD simulations in the absence and presence of an external static electric field with the field strength of 0.02, 0.06 and 0.1 V nm^{-1}, respectively. The fibril is kept in a ~8.7 × 8.7 × 8.7 nm^3 solvent box where orientation of each of the peptides is along the *Z* dimension. We apply the static electric field along the *Z* dimension and perform production run for 1 μs. In the presence of the 0.1 V nm^{-1} static electric field, we also investigate the

effect of harmonic positional restraint on the amino terminal nitrogen atom in each peptide fragment to mimic the role of membrane binding. We apply a harmonic positional restraint of 5000 kJ mol^{-1} nm^{-2} only along the Z dimension ($posres_z$) without any restraint along the XY dimension.

2.4 Assessment of the structural integrity of FUS-LC fibril

We investigate the stability of the β-fibril assembly of FUS-LC using three different measures, which are the fraction of native contacts, dipole moment of the fibril and the number of inter β strand hydrogen bonds. The fraction of native contacts[50] is defined as follows

$$F_N(t) = \frac{1}{|S|}\sum_{i,j\in S}\frac{1}{1+e^{\beta\left[r_{i,j}(t)-\lambda r^0_{i,j}\right]}} \quad (2)$$

where $F_N(t)$ is the fraction of native contacts at time t, S is the set of protein backbone atoms, $r_{i,j}(t)$ is the distance between atom i and j at time t, $r^0_{i,j}$ is the distance between atom i and j at time $t = 0$. λ and β are constants and take the values of 1.8 and 50 nm^{-1}, respectively. We compute F_N as a function of time (t) and also the distribution of $F_N(t)$ for the 0.6–1.0 μs time window of all the protein–membrane trajectories. The dipole moment is computed using the gmx dipoles utility. The numbers of hydrogen bonds are computed using MDAnalysis.[51] VMD[52] version 1.9.4 is used for visualization.

2.5 Metadynamics simulations

To probe the effect of a surface on intermolecular interactions between solutes, we calculate the PMF of an ion pair (Na^+–Cl^-) and a pair of simple dipolar hydrogen bond (HB) forming molecules (formamide), by employing well-tempered metadynamics.[53] We construct three different 5 nm × 5 nm surfaces for this purpose. The surfaces have three layers as shown in Fig. 5C. (a) Surf-1: negatively charged lower surface (shown in grey) where each bead possesses $q = -0.0346$. The two upper surfaces (shown in blue) are positively charged with each bead possessing $q = +0.0173$, to maintain the charge neutrality without counterions. (b) Surf-2: uncharged surface where every bead is individually neutral. (c) Surf-3: the three layers are decorated with alternating positive and negative charges. The charges are chosen based on the surface charge density of the lipid membranes. The surfaces are fixed along the XY plane, and the ions are fixed at a vertical distance of $h = 0.5$ nm from the upper surface. For the ion pair PMFs, we compared the charge scaling strategy (by a factor of 0.75)[54] with the unscaled charmm36m parameters. All the ion pair PMFs are discussed in Fig. S17.†

For the formamide molecules, the vertical distances of the heavy atoms (*i.e.*, C, N, and O) are fixed at $h = 0.4$ nm. However, they are free to move along the X and Y directions. We choose the center of mass distance (r) as the collective variable. The height and width of the Gaussian deposits are 0.5 kJ mol^{-1} and 0.01 nm, respectively. The hills are deposited with a frequency of 1.2 ps. A metadynamics bias-factor of 5.0 is used at $T = 303.15$ K. The metadynamics simulations are run for over 200 ns to ensure convergence. The other parameters are the same as detailed in the atomistic MD simulation subsection.

3 Results

3.1 Stability of the fibrillar assembly of FUS-LC depends on the length of the peptide and the network of hydrogen bonds between fragments

The FUS-LC domain (residues 1–214) contains primarily polar residues (Q, S, Y, G, T) and P without any large hydrophobic residues such as I, L, V or F, and remains disordered in the monomeric state.[55] However, it forms amyloid like aggregates at 50 μM concentration where only a specific segment of 57 N-terminal residues (39–95) participates and produces an S shaped topology.[28] The rest of the residues remain disordered and create a fuzzy coat around the fibril. In the absence of the N-terminal half, residues 112–150 form a U shaped assembly of β hairpin (FUS-LC-C). Using atomistic MD simulations, it was shown that the FUS-LC-C fibril comprising 10 fragment copies remained intact over 500 ns of simulation and was stabilized by a diverse set of hydrogen bonded networks.[29] To examine the surface induced stability of FUS-LC, we choose a starting configuration that loses its structural assembly in a computationally tractable time frame (∼1 μs). The peptide assembly of FUS-LC-C serves as a good starting point for this purpose as we can systematically modulate its stability by decreasing the number of monomers or peptide length.

First, we prepare a construct that contains only 4 monomers and perform simulations in bulk solution. We find that the assembly remains intact on the μs timescale (Fig. 1A) where the Cα–Cα contact map (Fig. 1B) reveals a stable network of inter-β-strands hydrogen bonds. Since each of the monomers remains in a β-hairpin, additional intra-β-strand contacts appear in the directions perpendicular to that of inter-β-strands contacts. We then truncate the length of the peptide by considering only the 19 residues from the N-terminus (residue: 112–130) and construct a 8-fragment structure by coordinate replication so that the total number of contacts remains similar to that in the previous case (Fig. 1A). We adjust the solvent box size in such a way that the peptide assembly remains periodic along the Y-direction. Under this continuous arrangement, the peptide assembly again shows stability over the μs timescale as evident from the contact map (Fig. 1C and D) and the time evolution of the fraction of native contacts (Fig. 1F). However, once we add solvent padding around the fibril to break the periodicity along Y (Fig. 1E), we observe a rapid decay in the number of contacts within 500 ns (Fig. 1G). Subsequently, the ordered assembly of β-strands collapses into a disordered state that only maintains 30% of its native backbone contacts (Fig. 1F); the presence of one hydrophobic residue (PRO) per peptide prevents the fibril from disassembling completely (Fig. S4†). Thus, we identify that competition in hydrogen bonding by the solvent molecules around the discontinuous β-fibril model is the primary reason for its reduced stability, and that it serves as a good starting construct to study how membrane/air–water interfaces impact on its stability.

3.2 Anionic membrane stabilizes the β-fibril assembly of FUS-LC

We carry out MD simulations of the truncated 8-fragment β-fibril assembly (residue 112–130) of FUS-LC (as shown in Fig. 1E) in the presence of membranes composed of either fully zwitterionic (DOPC) or anionic(DOPG/DOPS) lipids. We explore in total 5 initial orientations of the fibril with respect to the membrane plane (Fig. 2A and S1†). With anionic lipids (DOPG/DOPS), the peptide assembly remains ordered, maintaining the fraction of native backbone contacts ≥0.6 (Fig. 2B) over the time course of the simulation. By contrast, a membrane composed of zwitterionic lipids (DOPC) does not stabilize the β-fibril. In this case, decay of the fraction of native contacts follows a similar trend as that observed in bulk solution (Fig. 2B). By analyzing the rupture events strand-by-strand, we reveal a stochastic disassembly mechanism (Fig. S7†) in which the separation initiates at either terminal (blue) or core (red) pairs of peptide monomers in different trajectories.

The total dipole moment of the peptides serves as an alternate marker for the structural integrity and follows the same trend as the fraction of native contacts (Fig. 2C). The total dipole moment of the fibril decays by a small amount (∼2000 D to ∼1600 D) in the presence of anionic membranes whereas it decreases significantly (∼2000 D to ∼500 D) in the presence of a zwitterionic membrane and in bulk solution. We also

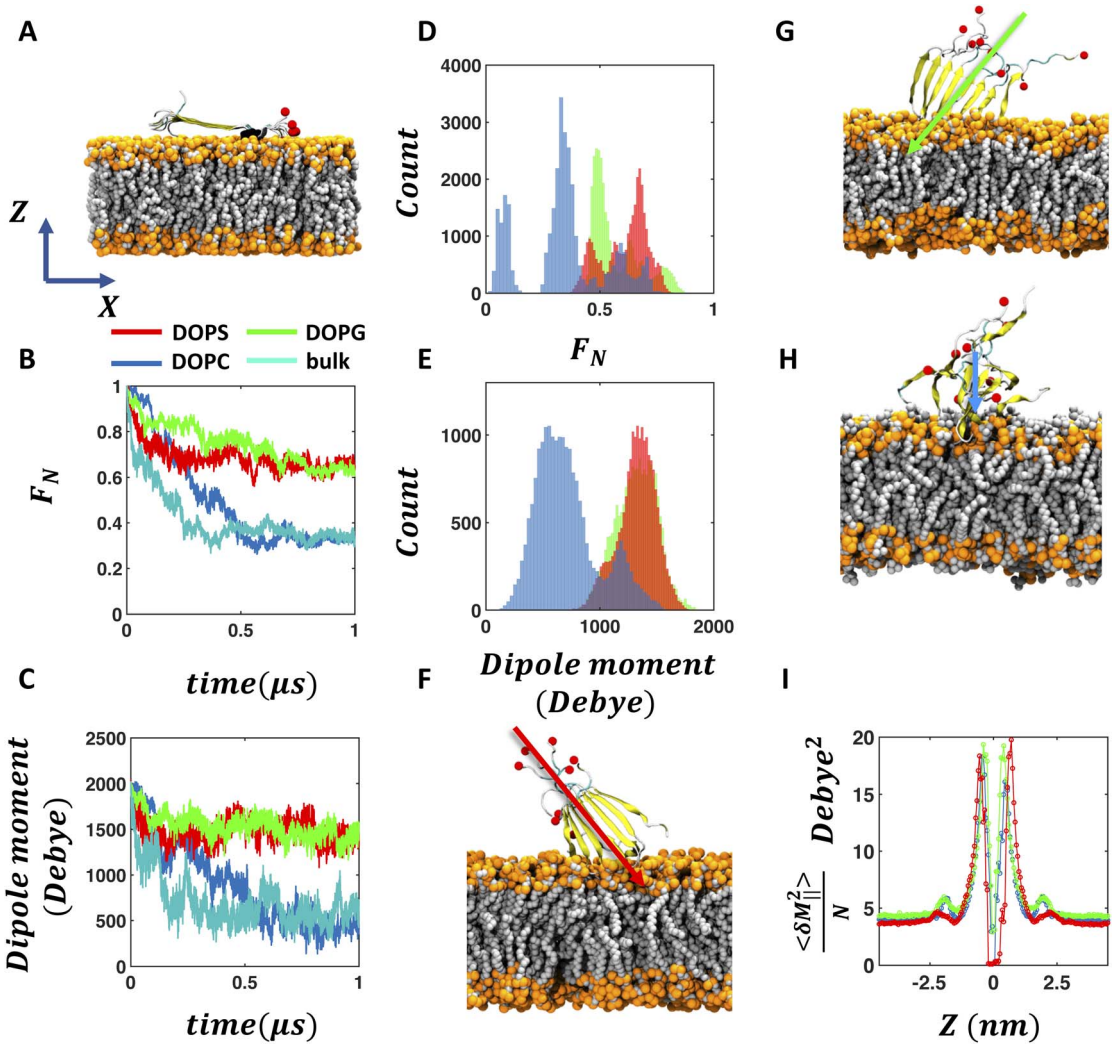

Fig. 2 Anionic membrane enhances the stability of the FUS-LC fibril. (A) Initial orientation of the FUS-LC fibril with respect to the membrane in one of the MD trajectories (see Fig. S1† for all the initial conformations). Proline is the only hydrophobic residue present in this sequence of FUS-LC and is highlighted in black. The red spheres indicate the C-terminal oxygen atoms (OT1) in each fragment. (B) Representative time evolution trace of the fraction of native contacts of FUS-LC in the presence of DOPS, DOPG, DOPC membranes and in the absence of any membrane. (C) Evolution of the dipole moment magnitude of the FUS-LC fibril in the same trajectories as shown in B. (D and E) Distribution of the fraction of native contacts and magnitude of the dipole moment obtained from 0.6–1.0 μs segments of all the five trajectories. Snapshots of FUS-LC fibril on (F) DOPS (G) DOPG and (H) DOPC membranes after 1.0 μs of MD simulation for the trajectory shown in A–C. (I) Grid-wise dipole moment fluctuations of water molecules parallel to the membrane (perpendicular components in Fig. S6†) computed for different layers along the Z axis (membrane normal) for the three membrane cases. A diminished second peak near $|Z| \sim 2.5$ nm distinguishes DOPS from DOPG and DOPC, indicating the dissimilarity in the dielectric profile near PS *vs.* PG membrane surfaces.

compute the distributions of the fraction of native contacts and the dipole moment from the 0.6–1 μs segments of all trajectories. The results further demonstrate the statistical significance of our observation that anionic membranes significantly enhance the stability of the FUS-LC fibril while a zwitterionic membrane fails to do so (Fig. 2D and E). Although the distributions of the fraction of native contacts in the presence of three membranes overlap with each other, their peak positions are distinct. In the presence of DOPC membrane, FUS-LC exhibits 0.35 as the most probable fraction of native contacts, as compared to the values of 0.48 and 0.67 for DOPG and DOPS membranes, respectively. In the case of dipole moment distribution, anionic membranes maintain high values (1320 ± 179 D for DOPG and 1324 ± 167 D for DOPS) compared to the case of a zwitterionic membrane (712 ± 276 D for DOPC). Further, we quantify the stability of FUS-LC by computing the number of inter β strand hydrogen bonds in the presence of the three membranes (Fig. S11†). We observe the highest number of backbone hydrogen bonds (Fig. S11A†) in the presence of DOPS (31 ± 6), followed by DOPG (29 ± 6) and DOPC (19 ± 7).

In all the trajectories, the fibril attaches to the anionic membrane through its positively charged amino terminus (representative snapshot after 1 μs simulation are shown in Fig. 2F–H; additional snapshots are shown in Fig. S2†). However, in the case of a zwitterionic membrane, FUS-LC does not exhibit any specific membrane anchoring residues (snapshot after 1 μs simulation is shown in Fig. 2H). Mass density profiles of phosphate planes of the membrane and TYR3 and TYR20 of the fibril also indicate an ordered vertical orientation of the fibril in the presence of anionic membranes but not in the presence of a zwitterionic membrane (Fig. S3†). Although the magnitude of the fibril's dipole moment is dependent on the nature of the interacting membrane, its direction remains similar in all cases and points towards the core of the membrane (arrows in Fig. 2F–H). In short, the fraction of native contacts, dipole moment, and hydrogen bond analysis consistently support the distinct structural features of FUS-LC on anionic *vs.* zwitterionic lipid membranes. To understand the molecular origin of such dependence, we examine the key characteristics that distinguish the water interfaces of the three membranes.

We compute the 2D joint probability distributions of $\cos\theta$ and Z position of water molecules for the three types of membrane simulations (Fig. S5†) where θ represents the angle between the dipole moment vector of each water molecule and the Z axis (*i.e.*, the membrane normal). We confirm a local alignment of water molecules at the anionic membrane surface as evident from the high probability density of $\cos\theta = \pm 1$ near the DOPS/DOPG-water interface ($Z = \pm 2.5$–3 nm). On the other hand, DOPC shows a uniform probability distribution of $\cos\theta$ at the interface. The distinct water orientation at the anionic membrane water interface reflects the local electric field that may serve as a key factor to orient and stabilize the β-fibril assembly of FUS-LC, a hypothesis that we explore below. To explain the enhanced stabilization of the fibril in the presence of DOPS membrane compared to DOPG, we monitor the polarization fluctuation profile of the water molecules near the surface. The fluctuation of the parallel component of the water dipole is significantly lower at the DOPS/water interface as compared to DOPG/DOPC (Fig. 2I). This distinct polarization profile of the DOPS membrane, which is correlated to the effective dielectric screening in the direction parallel to the interface, may play a role in stabilizing the fibril to a higher extent than DOPG (see Discussion).

3.3 Stability of the β-fibril assembly of FUS-LC at the air–water interface

To investigate whether the air water interface can stabilize the hydrogen bonded network of the β-fibril assembly of FUS-LC, we place the fibril at the air–water interface (Fig. 3A) and employ flat bottom positional restraints on the peptide and water molecules to keep the peptides at the interface (interface-4). The fibril maintains its stability (Fig. 3B) as evident from the high fraction of native contacts (0.68–0.87, see Fig. 3C) and the dipole moment (Fig. 3D). Without any positional restraint on the peptides or water molecules (bulk-2 in Fig. 3C, D and S8–S10†), the fibril quickly inserts into the bulk water layer as the 19-residue peptide segment mostly contains hydrophilic residues except one proline, which is not sufficient to keep the fibril at the interface. As a result, the fibril experiences a bulk-like environment, leading to a rapid dissociation of the peptide assembly as observed in regular bulk (bulk-1) simulations (Fig. 3C and D). In fact, applying a flat bottom positional restraint to the peptides alone is also not sufficient, as water molecules freely wrap around the peptides to create a bulk like environment (bulk-3 in Fig. S8–S10†), leading to the disassembly of the β-fibril.

To understand the origin of enhanced stability of the fibril at the air–water interface, we note that water molecules are known to exhibit dangling O–H bonds that do not participate in hydrogen bonding with other water molecules at the interface.[56,57] In other words, interfacial water molecules exhibit preferential orientations, as reflected by the non-zero average $\cos\theta$ values at the interface (Fig. 3E), where θ is the angle between the water dipole and the interface normal; $\langle\cos\theta\rangle$ reaches up to 0.1 on the peptide-containing interface and 0.06 on the peptide-free interface. We further quantify the interfacial water structure by computing the distribution of $\cos\theta_H$ where θ_H is the angle between the O–H bond vector with respect to the Z axis. Due to the presence of dangling O–H bonds at the air–water interface, the population of the two O–H bond vectors can be resolved as separate peaks in the distribution of $\cos\theta_H$ (Fig. 3F). Such bimodal distribution of $\cos\theta_H$ becomes enhanced (Fig. S12I–L† *vs.* M–P) at the peptide containing interface, further confirming that the peptides induce alignment of the interfacial water layer. These results are qualitatively consistent with observations from recent SFG experiments that FUS-LC fibril induced local ordering of water molecules, as inferred from the sign flip and blue peak shifts in Im χ^2.[23] Such aligned water molecules create a local electric field at the air–water interface. In the next section, we investigate whether an external static electric field in bulk water has any impact on the stability of the β-fibril.

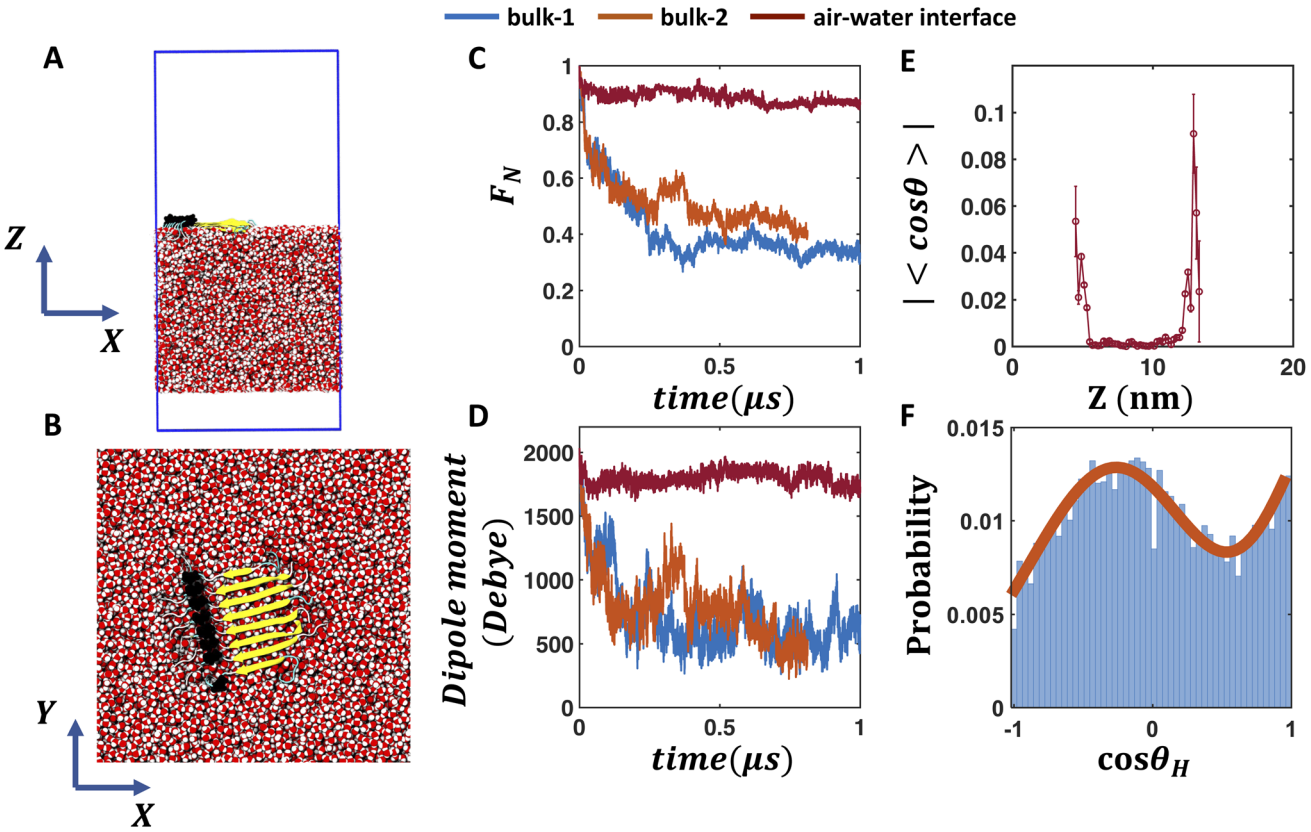

Fig. 3 FUS-LC fibril at the air–water interface. (A and B) Side and top views of the FUS-LC fibril at the air–water interface. The blue box represents the PBC boundary. Flat bottom positional restraints are applied on peptide and water molecules to keep the peptides at the interface. (C and D) The fraction of native contacts of the FUS-LC fibril and its dipole moment magnitude *vs.* time for two bulk and one air–water interface simulations. FUS-LC at the air–water interface exhibits high stability whereas the peptide assembly dissociates in all bulk simulations. (E) Absolute value of the average $\cos\theta$ of water molecules at different Z positions (with a grid resolution of 5 Å) of the simulation box for the interface trajectory. Standard error of $\langle\cos\theta\rangle$ is shown as error bar. θ is the angle between the water dipole moment vector and the Z axis. Non-zero average $\cos\theta$ values at the air–water interface indicate local alignment of water, which is enhanced in the FUS-LC containing interface. Data from other air–water interface simulations are shown in the ESI.† The air–water interface shown here is termed as interface-4 in Fig. S8–S10.† (F) Angular distribution of the O–H bond vectors of water molecules at the peptide-containing interface. Here, θ_H is the angle between an O–H bond vector and the Z axis. The two O–H bond vectors in each water molecule can be resolved at the interface, leading to a bimodal distribution of $\cos\theta_H$. By contrast, bulk water molecules (Fig. S10I and M†) produce uniform distributions of $\cos\theta_H$.

3.4 Effect of electric field on the stability of the β-fibril assembly of FUS-LC

Both anionic membrane-water and air–water interfaces exhibit considerable local electric fields, the magnitude of which decays from the interface to the bulk. Therefore, in this section, we aim to determine whether we can recreate the impact of these interfaces on the stability of the FUS-LC fibril by applying an external electric field in bulk water. Since a spatially heterogeneous electric field is less straightforward to implement, we study the impact of a spatially homogeneous electric field on the stability of the fibril. In case of folded globular proteins like ubiquitin, a weak electric field (0.1–0.5 V nm^{-1}) does not disrupt the structural fold whereas a strong electric field of 1–2 V nm^{-1} leads to unfolding.[58] On the other hand, amyloid β fibril disintegrates within 100 ns in the presence of as low as 0.2 V nm^{-1} electric field.[59] We explore a weak electric field of 0–0.1 V nm^{-1} to study the impact on the stability of the β-fibril assembly of FUS-LC. We supply the electric field along the Z direction which is also the direction of the dipole moment of the peptide assembly. As shown in Fig. 4A, we do not observe any additional stability of the β-fibril in the presence of an electric field in the bulk (Fig. S13A–C†). The fraction of native contacts decays by 60% within 500 ns of simulation in all cases, somewhat slower compared to the case without any electric field (Fig. S13B†).

We note that the anionic membranes provide an anchoring platform for the peptides in addition to the local electric field at the membrane–water interface. Peptides remain attached to the membrane through their positively charged amino termini. To mimic this effect, we apply harmonic positional restraints in addition to the electric field such that movement of the amino terminal atoms are restricted along the direction (Z-axis) of the electric field. In the presence of such restraints ($posres_z$ = 5000 kJ mol^{-1} nm^{-2} $posres_{x,y}$ = 0), 0.1 V nm^{-1} electric field significantly improves the stability of the peptide assembly compared to that in the absence of the electric field (Fig. 4A and B). The fraction of native contacts increases to 0.65 from the value of 0.32 observed in the case of field-free and restraint-free

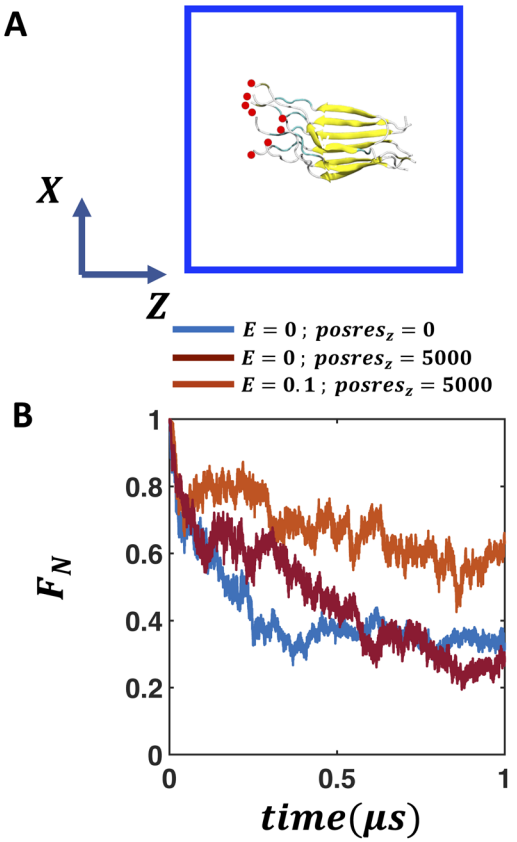

Fig. 4 Electric field induced stability of the FUS-LC fibril in bulk solution. (A) Snapshots of the FUS-LC fibril in the presence of an external electric field (0.1 V nm^{-1}) along the Z axis and in the presence of harmonic positional restraints (5000 kJ mol^{-1} nm^{-2}) along the direction of the external electric field. The simulation box is represented by a blue square. (B) The fraction of native contacts with respect to the timescale of simulation indicate that in the presence of external electric field and position restraints along the direction of the field enhances the stability of the fibril. For comparison, the fraction of native contacts in the absence of any electric field or positional restraints is also shown (deep cyan). Applying harmonic positional restraints on the amino terminus of the peptides does not lead to any enhanced structural stability in the absence of an electric field (maroon).

simulation after 1 μs. As a control simulation, only applying positional restraints along the Z-axis in the absence of any electric field ($E = 0$ V nm^{-1}, Fig. 4B) leads to a rapid decay of the fraction of native contacts. Thus, both the electric field and positional restraints along the electric field direction are essential to the enhancement of structural integrity of the peptide assembly. Based on these observations, we expect a similar stabilizing effect in the presence of a heterogeneous electric field, where the degree of peptide alignment varies depending on the magnitude of the local electric field.

3.5 Enhanced hydrogen-bonding and electrostatic interactions near a surface

To understand the stabilizing effect of a surface from a free-energetic perspective, we study the potential of mean forces (PMFs) of simple systems near different surfaces and compare them with the bulk. All the surfaces exhibit a thin layer of aligned interfacial water network irrespective of the charge patterning (Fig. S15†).

As the β-sheets are stabilized by hydrogen bonds between peptide backbones, we study a pair of formamide molecules that can form multiple peptide-like hydrogen bonds (C=O···H–N). The PMF is calculated with respect to their center-of-mass distance by keeping the non-hydrogen atoms (C, N, and O) in the same plane, and at a distance of 0.4 nm from the surface. In the absence of a surface, the same constraints are used on the non-H atoms. In Fig. 5A, we plot the PMFs of the four systems. In the bulk, the PMF profile shows a single shallow and broad basin that corresponds to a singly hydrogen-bonded state (Fig. 5C). Interestingly, near a surface, another basin at lower r (~0.33 nm) appears that corresponds to a doubly hydrogen bonded configuration (shown in Fig. 5B), in addition to the broader basin around r ~0.45 nm. The convergence tests of the well-tempered metadynamics simulations are provided in Fig. S18.†

To evaluate the stability of ionic electrostatic interactions, we calculate the PMFs for an ion pair in different environments

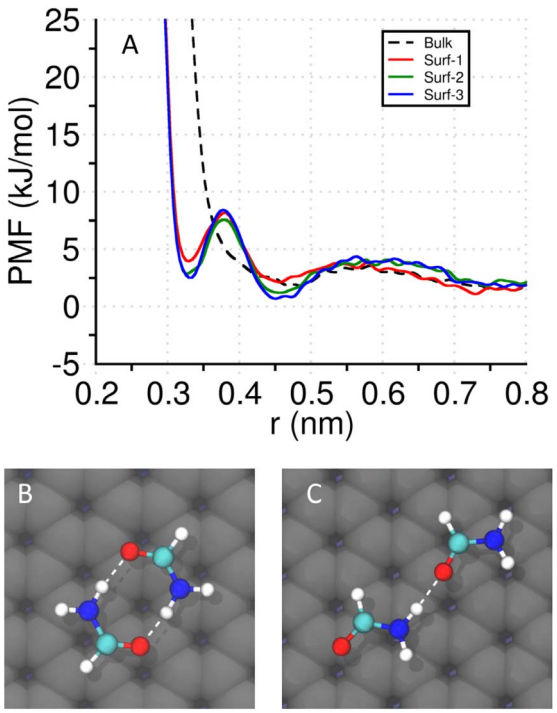

Fig. 5 Potentials of mean force (PMFs) of two formamide molecules with respect to the center-of-mass distance (r), in the absence (bulk/water) and presence of different surfaces (surf-1: negatively charged, surf-2: uncharged, and surf-3: mixed/alternating positive and negative charges). The surface contains three layers to balance the surface charge distribution without adding counterions. (A) PMFs of a pair of formamide in the bulk (dashed line) and in the presence of three different surfaces. A minimum at $r \sim 0.33$ nm (absent in bulk) is observed when the molecules are close to an interface. In all four systems, the second minimum ($r \sim 0.45$ nm) is present. (B) A doubly hydrogen-bonded configuration of two formamides corresponds to the first minimum at $r \sim 0.33$ nm. (C) A singly hydrogen-bonded configuration of two formamide molecules that corresponds to the second minimum at $r \sim 0.45$ nm.

(Fig. S17†). We find that the PMFs are weakly dependent on the nature of the surface, and reveal a notable increase in the strength of ion-pair interaction near the surface relative to the bulk. This can be understood from the interfacial solvation profile where irrespective of the charge patterning of the surface, the interfacial water molecules align in a similar way unlike in the case of membrane-water interface (Fig. S5 *vs.* S15†). Furthermore, upon scaling the ionic charges (by a factor of 0.75),[54] the trend remains unchanged. However, both the free-energy barrier and the binding free-energy decrease, as compared to the unscaled charge model. The scaled charge model provides a better match with an earlier *ab initio* PMF.[60]

4 Discussion

In this study, we explicitly demonstrate that a planar β-fibril assembly of FUS-LC composed of 8 monomers (with 19 amino acid residues per monomer) undergoes spontaneous dissociation in bulk water but gains significant stabilization in the presence of anionic membrane surfaces and the air–water interface. The arrangement of water molecules at these interfaces leads to a uniquely solvated state that differs from the bulk solution. In separate simulations, we show that an external static electric field can alter the bulk solvation in the absence of any surface in a similar way and enhances the stability of the fibrillar assembly when the peptides are anchored. Further, we show the enhanced stabilization of an ion-pair and a pair of formamide molecules induced by static surfaces of various degrees of charge decoration and hydrophobicity. Taken together, our study supports a molecular mechanism of surface induced stabilization of a peptide assembly where interfacial solvation enhances the strength of the hydrogen bonded network among the peptides. The model captures the fundamental differences in intermolecular interactions due to the presence of surfaces of different kinds. The structural integrity in the model fibrillar segment studied here is expected to be different from that of the full length FUS-LC domain investigated in experiments. However, to extract insights in atomistic details, we begin with a smaller subset of peptide fragments and focus on the hydrogen bonding interactions to evaluate the impact of different interfaces, ranging from membrane (anionic *vs.* zwitterionic) to the air–water interface. This can be used as a starting point to comprehend how various surface chemistry can control the biomolecular association/dissociation.

The local alignment of the interfacial water layer at the anionic membrane- and air–water interfaces is a well characterized phenomenon using, for example, SFG spectroscopy. However, it is not clear how such aligned water structure contributes to the stabilization of certain intermolecular interactions that facilitates the formation of droplets/aggregates of IDPs. We provide insight in this regard by illustrating a prominent impact of interface on the association free energy profiles of ion-pair and hydrogen bonding interactions. The PMFs we computed for two simple systems near the surface and in the bulk reveal that surfaces can enhance the stability of ionic electrostatic interactions and hydrogen bonds between two dipolar molecules. The unique alignment of water dipoles at the interface is responsible for the general stabilizing effect observed here. Additionally, the incomplete solvation shell structure around an ion/dipole near an interface reduces its solvation enthalpy that serves as a driving force of ion-pair (or dipoles) association. In this context, Garde and co-workers showed that the binding energy of an ion-pair increases significantly as one moves from bulk to the air–water interface and eventually to vacuum.[38]

In particular, our findings shed light on two recent experimental results.[20,23] It was shown that anionic membranes composed of either DOPG or DOPS lipid molecules significantly reduced the concentration threshold required for the condensation of FUS-LC while no reduction was observed in the case of a zwitterionic (DOPC) membrane. This is qualitatively consistent with our observation that the stability of the fibril is enhanced at the anionic membrane surface compared to the zwitterionic membrane (Fig. 2). Using vibrational Sum Frequency Generation (SFG) spectroscopy, it was further demonstrated that DOPS induced local ordering of the FUS-LC leading to β sheet like structures while DOPG does not produce any such structural ordering despite also catalyzing the condensation. This is also in line with our simulation result where we capture a higher fraction of native contacts and a higher number of inter-peptide hydrogen bonds in the presence of DOPS compared to DOPG (Fig. 2D and S11A†). We show that DOPS, compared to DOPG, exhibits diminished fluctuation of the parallel component of water dipole near the surface (Fig. 2I). The fluctuations of the water dipole characterize the degree of dielectric screening,[61–63] thus the observation suggests that screening of electrostatic interactions parallel to the membrane surface is lower near the DOPS surface than DOPG, which might explain the more stable fibril β-assembly at the DOPS surface.

Our simulations reveal that FUS-LC attaches to the membrane with its positively charged amino terminus primarily driven by electrostatic interactions. This mode of attachment is different from that of typical curvature generating proteins which employ hydrophobic residues to insert into the membrane.[64] Since FUS-LC does not carry any large hydrophobic amino acids we expect that the electrostatics driven attachment with the membrane through the positively charged amino terminus prevails even in cases of longer segments (*e.g.*, the 1–163 segment as used in the experiment). Therefore, negatively charged membrane surfaces provide anchoring points for proteins and exhibit altered interfacial solvation to induce assembly of the proteins near the surface. This initial protein assembly on the surface of the anionic membrane can serve as nucleation template for further growth of the condensate.

The air–water interface is an interesting model hydrophobic–hydrophilic interface that can stimulate aggregation of FUS-LC leading to solid fibril like aggregate.[23] Although the reason for the accumulation of FUS-LC at the air–water interface is not well understood, it was hypothesized that the interface induced partitioning of hydrophobic/hydrophilic residues of FUS-LC. As a consequence of partitioning, hydrophilic residues promote local alignment of interfacial water molecules as was demonstrated using SFG spectra. Since the 19 residue fragment

of FUS-LC considered here contains only one hydrophobic residue, we do not observe any spontaneous partitioning of the fibril at the air–water interface. However, once we keep the fibril at the air–water interface by restricting the displacements of water and protein atoms, we capture enhanced stability of the fibril compared to that in the bulk water (Fig. 3C).

Regarding the physical factors that are essential to the stabilization effect, stability of alpha helix has been shown to be sensitive to the activity of nearby water, which is in turn modulated by the nature of the nearby surface.[65,66] On the other hand, desolvation of the hydrophobic residues and the reduction of the total air–water contact area were identified as the key determining factors for the stability gain of an amphipathic β-hairpin forming peptide at the air–water interface.[67] It was also demonstrated that the electrostatic interaction between an ion pair can be significantly altered at the liquid–vapor interface compared to that in the bulk solution.[38] While partial desolvation likely contributes to the enhanced stability of FUS-LC β-fibril at the air–water interface, we note that the structure becomes significantly distorted in a vacuum simulation (Fig. S16†). Our findings indicate that the partial solvation of the fibril at the air–water interface is not sufficient to break the inter β strand hydrogen bonds but the hydrophilic sidechains of the amino acid residues can form hydrogen bonds with the available water molecules. As a result, the interfacial water layer that includes the fibril shows a higher extent of ordering than the other interface (Fig. 3E, S9 and S12I–L *vs.* M–P†). Therefore, the restricted exposure of the FUS-LC fibril towards water at the air–water interface facilitates the formation of hydrogen bonds between peptide residues and water molecules in such a way that the fibril does not collapse as observed in vacuum and bulk solutions.

Interfaces are known to exhibit local electric fields whose magnitude can vary depending upon the nature of the interface. Membranes composed of cationic lipids have been shown to exhibit strong electric field at the membrane–water interface.[35] In the case of a water–organic surfactant interface, the magnitude of electric field can be 1 V nm^{-1}.[37] To understand the interface driven condensation/aggregation, it is thus important to understand the effect of an external electric field on the conformations and dynamics of LLPS forming IDPs. In the case of amyloid β, 0.2 V nm^{-1} electric field induced the formation of β hairpin conformation, which is believed to be an important intermediate state during aggregation.[68] Further, amyloid β oligomer comprising residue 16–42 was found to be resilient to 0.5 V nm^{-1} electric field for at least 50 ns.[69] We study the stability of FUS-LC fibril on the μs timescale and find that the application of an electric field alone does not yield additional stabilization (Fig. 4B). Although the presence of an external electric field alters the water structure (Fig. S14C†), it induces a shear stress along the direction of the applied field, leading to a rupture of the fibril. When positional restraints on the amino terminus of the peptide are applied to mimic peptide binding to an anionic membrane, the external electric field is observed to enhance the stability of FUS-LC (Fig. 4D, S14A and B†) by aligning the peptides in the same direction. Therefore, the impact of an electric field on peptide assembly is context dependent.

5 Conclusion

Different interfaces have been shown in recent experiments to have a major impact on the processes of protein LLPS and aggregation. However, a unifying molecular mechanism that explains the effects due to surfaces of different levels of hydrophobicity and charge patterning has not been established. Using a model fragment of the FUS-LC β-fibril (residues 112–130), our study highlights the role of interfacial solvation at the membrane–water and air–water interfaces in enhancing the stability of peptide assemblies. The different effects for DOPS and DOPG observed in both experiments[20] and our simulations underscore the importance of specific chemical interactions beyond generic electrostatics to the interfacial solvation and therefore processes that occur at those interfaces. The liquid droplet state formed by FUS-LC in bulk solution involves a complex network of interactions including hydrogen bonding, π–sp^2, and hydrophobic interactions.[26] On the other hand, π–π stacking among the aromatic (Y) residues have been shown to stabilize the fibrillar structure of FUS-LC.[70] The planar β-fibril assembly of FUS-LC considered here serves as a starting point to study the impact of interfacial solvation on the hydrogen bonding interactions among the peptide strands. The phenomena of LLPS, hydrogel formation, and aggregation of FUS-LC are intricate processes that are interrelated and involve longer segments of residues with diverse forms of interactions. To understand such complicated processes it is imperative to employ efficient multiscale models that encompass essential physical and chemical interactions. The results of our research help highlight several physical factors that contribute to the effect of the interface on the condensation/aggregation of proteins rich in polar amino acids, while additional mechanisms are likely to contribute in the case of full length FUS-LC.

Data availability

Data for this article, including simulation trajectories, topologies, and analysis scripts are available at Zenodo in two parts. Part-1: **https://doi.org/10.1101/2024.01.15.575617** and URL – **https://zenodo.org/records/11974024**. Part-2: **https://doi.org/10.5281/zenodo.11935101** and URL – **https://zenodo.org/records/11935101**. The data supporting this article have also been included as part of the ESI.†

Author contributions

QC and SP conceived the presented idea. SM performed the metadynamics simulation and SP performed the rest of the simulations and analysis. IS carried out some initial part of the simulations. SP, SM and QC wrote the manuscript. QC supervised the project.

Conflicts of interest

There are no conflicts to declare.

Acknowledgements

The work is supported in part by the NSF grant to QC (CHE-2154804). This work used Delta at the National Center for Supercomputing Application (NCSA) through allocation MCB110014 from the Advanced Cyberinfrastructure Coordination Ecosystem: Services & Support (ACCESS) program,[71] which is supported by National Science Foundation grants #2138259, #2138286, #2138307, #2137603, and #2138296. A part of the computational work was performed on the Shared Computing Cluster which is administered by Boston University's Research Computing Services (URL: **https://www.bu.edu/tech/support/research/**). We thank Prof. John Straub for his valuable comments and suggestions on the manuscript.

Notes and references

1 S. F. Banani, H. O. Lee, A. A. Hyman and M. K. Rosen, *Nat. Rev. Mol. Cell Biol.*, 2017, **18**, 285–298.
2 Y. Shin and C. P. Brangwynne, *Science*, 2017, **357**, 1253.
3 B. Wang, L. Zhang, T. Dai, Z. Qin, H. Lu, L. Zhang, F. Zhou and S. Transd, *Targeted Ther.*, 2021, **6**, 290.
4 A. Zbinden, M. Pérez-Berlanga, P. De Rossi and M. Polymenidou, *Dev. Cell*, 2020, **55**, 45–68.
5 C. Mathieu, R. V. Pappu and J. P. Taylor, *Science*, 2020, **370**, 56–60.
6 S. Banjade and M. K. Rosen, *eLife*, 2014, **3**, e04123.
7 L. B. Case, *Nat. Cell Biol.*, 2022, **24**, 404–405.
8 W. T. Snead, A. P. Jalihal, T. M. Gerbich, I. Seim, Z. Hu and A. S. Gladfelter, *Nat. Cell Biol.*, 2022, **24**, 461–470.
9 A. P. Liu, D. L. Richmond, L. Maibaum, S. Pronk, P. L. Geissler and D. A. Fletcher, *Nat. Phys.*, 2008, **4**, 789–793.
10 E. N. Firat-Karalar and M. D. Welch, *Curr. Opin. Cell Biol.*, 2011, **23**, 4–13.
11 J. Stachowiak, F. Yuan, H. Alimohamadi, B. Bakka, A. Trementozzi, K. Day, N. Fawzi and P. Rangamani, *Proc. Natl. Acad. Sci. U.S.A.*, 2021, **118**, e2017435118.
12 M. B. Stone, S. A. Shelby, M. F. Nunez, K. Wisser and S. L. Veatch, *eLife*, 2017, **6**, e19891.
13 P. K. Auluck, G. Caraveo and S. Lindquist, *Annu. Rev. Cell Dev. Biol.*, 2010, **26**, 211–233.
14 G. Fusco, A. De Simone, P. Arosio, M. Vendruscolo, G. Veglia and C. M. Dobson, *Sci. Rep.*, 2016, **6**, 27125.
15 C. Galvagnion, A. K. Buell, G. Meisl, T. C. Michaels, M. Vendruscolo, T. P. Knowles and C. M. Dobson, *Nat. Chem. Biol.*, 2015, **11**, 229–234.
16 J. Habchi, S. Chia, C. Galvagnion, T. C. Michaels, M. M. Bellaiche, F. S. Ruggeri, M. Sanguanini, I. Idini, J. R. Kumita, E. Sparr, *et al.*, *Nat. Chem.*, 2018, **10**, 673–683.
17 S. Wegmann, B. Eftekharzadeh, K. Tepper, K. M. Zoltowska, R. E. Bennett, S. Dujardin, P. R. Laskowski, D. MacKenzie, T. Kamath, C. Commins, *et al.*, *EMBO J.*, 2018, **37**, e98049.
18 C. N. Chirita, M. Necula and J. Kuret, *J. Biol. Chem.*, 2003, **278**, 25644–25650.
19 H. Zhao, E. K. Tuominen and P. K. Kinnunen, *Biochemistry*, 2004, **43**, 10302–10307.
20 S. Chatterjee, D. Maltseva, Y. Kan, E. Hosseini, G. Gonella, M. Bonn and S. H. Parekh, *Sci. Adv.*, 2022, **8**, eabm7528.
21 B. O. Elenbaas, L. Khemtemourian, J. A. Killian and T. Sinnige, *Biochemistry*, 2022, **61**, 1465–1472.
22 Q. Zheng, S. N. Carty and N. D. Lazo, *Langmuir*, 2020, **36**, 8389–8397.
23 D. Maltseva, S. Chatterjee, C.-C. Yu, M. Brzezinski, Y. Nagata, G. Gonella, A. C. Murthy, J. C. Stachowiak, N. L. Fawzi, S. H. Parekh and M. Bonn, *Nat. Chem.*, 2023, **15**, 1146–1154.
24 C. Vance, B. Rogelj, T. Hortobágyi, K. J. De Vos, A. L. Nishimura, J. Sreedharan, X. Hu, B. Smith, D. Ruddy, P. Wright, *et al.*, *Science*, 2009, **323**, 1208–1211.
25 T. Matsumoto, K. Matsukawa, N. Watanabe, Y. Kishino, H. Kunugi, R. Ihara, T. Wakabayashi, T. Hashimoto and T. Iwatsubo, *Hum. Mol. Genet.*, 2018, **27**, 1353–1365.
26 A. C. Murthy, G. L. Dignon, Y. Kan, G. H. Zerze, S. H. Parekh, J. Mittal and N. L. Fawzi, *Nat. Struct. Mol. Biol.*, 2019, **26**, 637–648.
27 Y. Ji, F. Li and Y. Qiao, *J. Mater. Chem. B*, 2022, **10**, 8616–8628.
28 D. T. Murray, M. Kato, Y. Lin, K. R. Thurber, I. Hung, S. L. McKnight and R. Tycko, *Cell*, 2017, **171**, 615–627.
29 M. Lee, U. Ghosh, K. R. Thurber, M. Kato and R. Tycko, *Nat. Commun.*, 2020, **11**, 5735.
30 A. Kumar, D. Chakraborty, M. L. Mugnai, J. E. Straub and D. Thirumalai, *J. Phys. Chem. Lett.*, 2021, **12**, 9026–9032.
31 A. Garaizar, J. R. Espinosa, J. A. Joseph, G. Krainer, Y. Shen, T. P. Knowles and R. Collepardo-Guevara, *Proc. Natl. Acad. Sci. U.S.A.*, 2022, **119**, e2119800119.
32 Y. Shen, A. Chen, W. Wang, Y. Shen, F. S. Ruggeri, S. Aime, Z. Wang, S. Qamar, J. R. Espinosa, A. Garaizar, *et al.*, *Proc. Natl. Acad. Sci. U.S.A.*, 2023, **120**, e2301366120.
33 L. Emmanouilidis, E. Bartalucci, Y. Kan, M. Ijavi, M. E. Pérez, P. Afanasyev, D. Boehringer, J. Zehnder, S. H. Parekh, M. Bonn, *et al.*, *Nat. Chem. Biol.*, 2024, **20**, 1044–1052.
34 C. He, C. Y. Wu, W. Li and K. Xu, *J. Am. Chem. Soc.*, 2023, **145**, 24240–24248.
35 L. B. Dreier, Y. Nagata, H. Lutz, G. Gonella, J. Hunger, E. H. Backus and M. Bonn, *Sci. Adv.*, 2018, **4**, eaap7415.
36 F. Tang, T. Ohto, S. Sun, J. R. Rouxel, S. Imoto, E. H. Backus, S. Mukamel, M. Bonn and Y. Nagata, *Chem. Rev.*, 2020, **120**, 3633–3667.
37 R. Gera, H. J. Bakker, R. Franklin-Mergarejo, U. N. Morzan, G. Falciani, L. Bergamasco, J. Versluis, I. Sen, S. Dante, E. Chiavazzo, *et al.*, *J. Am. Chem. Soc.*, 2021, **143**, 15103–15112.
38 V. Venkateshwaran, S. Vembanur and S. Garde, *Proc. Natl. Acad. Sci. U.S.A.*, 2014, **111**, 8729–8734.
39 M. J. Abraham, T. Murtola, R. Schulz, S. Páll, J. C. Smith, B. Hess and E. Lindahl, *SoftwareX*, 2015, **1**, 19–25.
40 H. J. Berendsen, D. van der Spoel and R. van Drunen, *Comput. Phys. Commun.*, 1995, **91**, 43–56.
41 J. Huang, S. Rauscher, G. Nawrocki, T. Ran, M. Feig, B. L. De Groot, H. Grubmüller and A. D. MacKerell, *Nat. Methods*, 2017, **14**, 71–73.

42 B. R. Brooks, C. L. Brooks III, A. D. Mackerell Jr, L. Nilsson, R. J. Petrella, B. Roux, Y. Won, G. Archontis, C. Bartels, S. Boresch, *et al.*, *J. Comput. Chem.*, 2009, **30**, 1545–1614.
43 J. Lee, X. Cheng, J. M. Swails, M. S. Yeom, P. K. Eastman, J. A. Lemkul, S. Wei, J. Buckner, J. C. Jeong, Y. Qi, *et al.*, *J. Chem. Theory Comput.*, 2016, **12**, 405–413.
44 S. Jo, T. Kim, V. G. Iyer and W. Im, *J. Comput. Chem.*, 2008, **29**, 1859–1865.
45 T. Darden, D. York and L. Pedersen, *J. Chem. Phys.*, 1993, **98**, 10089–10092.
46 W. G. Hoover, *Phys. Rev. A*, 1985, **31**, 1695.
47 S. Nosé, *Mol. Phys.*, 1984, **52**, 255–268.
48 M. Parrinello and A. Rahman, *J. Appl. Phys.*, 1981, **52**, 7182–7190.
49 B. Hess, H. Bekker, H. J. Berendsen and J. G. Fraaije, *J. Comput. Chem.*, 1997, **18**, 1463–1472.
50 R. B. Best, G. Hummer and W. A. Eaton, *Proc. Natl. Acad. Sci. U.S.A.*, 2013, **110**, 17874–17879.
51 N. Michaud-Agrawal, E. J. Denning, T. B. Woolf and O. Beckstein, *J. Comput. Chem.*, 2011, **32**, 2319–2327.
52 W. Humphrey, A. Dalke and K. Schulten, *J. Mol. Graphics*, 1996, **14**, 33–38.
53 A. Barducci, G. Bussi and M. Parrinello, *Phys. Rev. Lett.*, 2008, **100**, 020603.
54 B. J. Kirby and P. Jungwirth, *J. Phys. Chem. Lett.*, 2019, **10**, 7531–7536.
55 K. A. Burke, A. M. Janke, C. L. Rhine and N. L. Fawzi, *Mol. Cell*, 2015, **60**, 231–241.
56 F. Tang, T. Ohto, T. Hasegawa, W. J. Xie, L. Xu, M. Bonn and Y. Nagata, *J. Chem. Theory Comput.*, 2018, **14**, 357–364.
57 Y. Fan, X. Chen, L. Yang, P. S. Cremer and Y. Q. Gao, *J. Phys. Chem. B*, 2009, **113**, 11672–11679.
58 A. Chakraborty and R. Venkatramani, *ChemPhysChem*, 2023, **24**, e202200646.
59 S. Muscat, F. Stojceski and A. Danani, *J. Mol. Graphics Modell.*, 2020, **96**, 107535.
60 J. Timko, D. Bucher and S. Kuyucak, *J. Chem. Phys.*, 2010, **132**, 114510.
61 S. Mondal and B. Bagchi, *Nano Lett.*, 2020, **20**, 8959–8964.
62 S. Mondal and B. Bagchi, *J. Chem. Phys.*, 2021, **154**, 044501.
63 D. J. Bonthuis, S. Gekle and R. R. Netz, *Langmuir*, 2012, **28**, 7679–7694.
64 S. Paul, A. Audhya and Q. Cui, *Proc. Natl. Acad. Sci. U.S.A.*, 2023, **120**, e2212513120.
65 H.-X. Zhou, *J. Chem. Phys.*, 2007, **127**, 245101.
66 E. J. Sorin and V. S. Pande, *J. Am. Chem. Soc.*, 2006, **128**, 6316–6317.
67 O. Engin and M. Sayar, *J. Phys. Chem. B*, 2012, **116**, 2198–2207.
68 Y. Lu, X.-F. Shi, F. R. Salsbury and P. Derreumaux, *J. Chem. Phys.*, 2017, **146**, 145101.
69 F. Lugli, F. Toschi, F. Biscarini and F. Zerbetto, *J. Chem. Theory Comput.*, 2010, **6**, 3516–3526.
70 D. Thirumalai, A. Kumar, D. Chakraborty, J. E. Straub and M. L. Mugnai, *Biopolymers*, 2023, e23558.
71 T. J. Boerner, S. Deems, T. R. Furlani, S. L. Knuth and J. Towns, *Practice and Experience in Advanced Research Computing (PEARC '23)*, 2023.